Single-crystalline MoO$_3$/functionalized multiwalled carbon nanotube nanocomposites for sensing phenothiazine in biological samples

Balamurugan Arumugam[a], Selvakumar Palanisamy[b*], Sayee Kannan Ramaraj[a*], Matteo Chiesa[b,c*]

[a]PG & Research Department of Chemistry, Thiagarajar College, Madurai-625009, Tamil Nadu, India.

[b]Laboratory for Energy Laboratory for Energy and NanoScience (LENS), Khalifa University of Science and Technology, Masdar Campus, PO Box, 54224, Abu Dhabi, United Arab Emirates.

[c]Department of Physics and Technology, UiT The Artic University of Norway, 9010, Tromso, Norway.

*Corresponding Authors

Dr. Selvakumar Palanisamy, Email: prmselva@gmail.com

Dr. Sayee Kannan Ramaraj, E-mail: sayeekannanramaraj@gmail.com

Prof. Matteo Chiesa, Email: matteo.chiesa@ku.ac.ae

Abstract

The increasing use of pharmaceutical medications has serious negative repercussions on the environment and human health. Here, a hydrothermal technique was employed to generate a single-crystalline molybdenum trioxide (MoO_3)/multi-walled carbon nanotubes (MoO_3/f-MWCNTs) nanocomposite that was then used as a novel electrode material for the electrochemical detection of phenothiazine (PTZ). Extensive characterization of the MoO_3/f-MWCNTs nanocomposite is reported by means of spectroscopic and microscopic techniques. The electrode modified with the MoO_3/f-MWCNTs nanocomposite displays superior electrocatalytic activity and lower oxidation overpotential (0.492 V vs.Ag/AgCl) to PTZ compared to benchmarking electrodes modified with MoO_3 and f-MWCNTs, respectively. Electrodes performance is evaluated by means of differential pulse voltammetry that reveals a low detection limit (7 nM), more comprehensive linear response range (up to 226 µM), and superior sensitivity (2.04 µA µM^{-1} cm^{-2}). The MoO_3/f-MWCNTs nanocomposite electrode can also detect PTZ in the presence of several biological compounds and metal ions in various aqueous environments demonstrating the sensing practicality.

Keywords: Single-crystalline; MoO_3 nanorods; Functionalized carbon nanotubes; Electroactive composite material; Phenothiazine, Electroanalysis

1. Introduction

In the global environment, active dyes, organic compounds, heavy metals, and pharmaceutical ingredients can negatively impact ecosystems and cause public health problems [1-3]. Environmental exposure to pharmaceutical ingredients is among the various pollutants that harm humans and ecosystems. Phenothiazine (PTZ), which has the chemical formula $S(C_6H_4)2NH$, is a heterocyclic molecule that belongs to the thiazine family and is used in medicinal chemistry. Due to their bioactivity and archetypal pharmacological features, PTZ compounds have been widely employed to treat various ailments and diseases. Over the past ten years, hundreds of medications, including promethazine, chlorpromazine, and prochlorperazine, have been identified from the basic PTZ structure [4,5]. PTZ is one of the most commonly prescribed psychotropic medicines, as well as a medication used to treat HIV infections [6]. The PTZ is used for producing organic dyes such as methylene blue, toluidine blue, and azure dye, as well as batteries and OLED displays. In addition to being used in the production of NADH, PTZ facilitates the production of polymers through electropolymerization, serves as an electrocatalyst in the determination of NADH, and is used in microelectronics as a donor unit and as a hole transporter in solar cells due to its electron-rich nitrogen and sulfur atoms [7-10]. PTZ is a drug that has a variety of medicinal actions, including antimalarial, anticancer, antihistaminic [11, 12], sedative, anti-tuberculosis [13], anti-psychotic, anti-anesthetic, and antiemetic activities [14]. Owing to its boat conformation, PTZ possesses both conventional and thermally activated delayed fluorophores (TADF) with different properties and molecular stuffing motifs. It has also been used in nucleophilic alkoxylation of alkyl olefins, photo redox-catalyzed C–N, and C–H/C–H cross-coupling reactions [15]. The prolonged use and excessive dosage of PTZ in various formulations have been associated with complications, such as cardiac issues, endocrine dysfunction, and reproductive system damage. A continuous intake of PTZ can also result in central nervous system damage, akathisia, tardive dyskinesia, hyperprolactinemia, and abnormal weight gain [5, 16-18]. Moreover, PTZ has been extensively

metabolized in the liver via cytochrome P-450 isoforms and mainly supports growth through ring-hydroxylation, S-oxidation, and N-demethylation [19, 20].

In recent years, developing sensitive and selective techniques for determining PTZ is an important research topic for various fields. The determination of PTZ can be accomplished using various methods, including spectrophotometry [21], liquid chromatography [22], and electrochemical methods [14,23]. The electrochemical method seems to hold the highest potential among these methods due to their fast response time, high accuracy, high sensitivity, selectivity, and cost-effectiveness. Modifying the electrode surface can significantly increase the efficiency of these electrochemical procedures, resulting in improved diagnostic signals that are reliable and sensitive. Consequently, significant efforts have been undertaken to improve sensor behavior, such as electron transport kinetics and detection limits [24,25]. Nanomaterials can offer valuable suggestions for electroanalysis by utilizing certain features that are achieved at the nanoscale, as demonstrated by substantial developments in nanotechnology.

Nanoscale transition metal oxides (TMOs) have gained considerable attention in recent years due to their chemical, optical, mechanical, semiconductor (n or p-type), and electrical properties, as well as their potential applications in energy storage devices, sensors, and photocatalysts [26, 27]. Among all TMOs, molybdenum trioxides (MoO_3) possess thermal stability, photocatalytic, and electrocatalytic properties, including high catalytic activity, low operation potential, and biocompatibility. As a result of these properties, MoO_3 is useful in a wide range of applications, such as batteries, sensors, photocatalytic activity, supercapacitors, dye-sensitized solar cells, and fuel cells [28-33]. Many polymorphous natural properties are associated with MoO_3, among them the orthorhombic α-MoO_3, which is thermodynamically stable, and the hexagonal MoO_3 is metastable. A MoO_3 sheet is formed by stacking several MoO_6 octahedrons with van der Waals forces, resulting in an anisotropic layered structure [34]. As a result of this nature, molybdenum ions easily produce oxygen vacancies, making them excellent materials for electrodes in sensors. Nevertheless, MoO_3 has some drawbacks, such as aggregation, and is less stable on electrode surfaces. Electrode

4

modifications using MoO3 entrapped carbon materials have been used to address the above issue. Carbon-based materials can be used as conductive materials and supporting matrices for various applications [35-40]. Multi-walled carbon nanotubes (MWCNTs) have excellent electrocatalytic properties, such as a large surface-to-volume ratio, low density, and high conductivity. However, MWCNTs have low solubility and dispersibility in many solvents, resulting in self-aggregation, and are inherently unsuitable for most applications. As a result, functionalizing MWCNTs before use ensures homogeneous dispersion and maximizes the surface properties of MWCNTs [41-44]. By integrating MoO_3 on the *f*-MWCNTs surface, the electrochemical response properties of both MoO_3 and *f*-MWCNTs will be enhanced for the electrochemical detection of PTZ.

In the current study, we describe for the first time a simple hydrothermal synthesis of a MoO_3/*f*-MWCNTs nanocomposite for reliable and sensitive electrochemical detection of PTZ. Crystallographic and spectroscopic studies confirm the successful synthesis of MoO_3, *f*-MWCNTs, and MoO_3/*f*-MWCNTs nanocomposite. The various electrode materials' electrochemical performance and electrocatalytic properties were examined using cyclic voltammetry (CV) and differential pulse voltammetry (DPV). By improving electron transport kinetics, electrical conductivity, active surface area, and functional active sites, the MoO_3/*f*-MWCNTs nanocomposite modified electrode performs better for PTZ detection than pristine MoO_3 and *f*-MWCNTs modified electrode. The MoO_3/*f*-MWCNTs nanocomposite electrode-based PTZ sensor exhibits a low detection limit, a broad dynamic response range, and great sensitivity, selectivity, and repeatability. Moreover, the developed sensor was used to measure the concentration of PTZ in the human urine and blood serum samples.

2. Experimental methods

2.1. Materials and methods

$Na_2MoO_4.2H_2O$, MWCNTs (50-90 nm diameter, >95% carbon basis), Con.HNO_3, ethylene glycol, and phenothiazine are of analytical grade and purchased from Sigma Aldrich. Multiwalled carbon nanotubes with

an outer diameter of 12–30 nm were purchased from Sigma-Aldrich. Disodium and monosodium phosphates were purchased from Alfa Aesar chemicals, and all the chemicals are analytical grade and used without further purification. All required solutions were prepared using double distilled (DD) water.

The structure and crystallinity of the synthesized materials were analyzed using XRD Xpert3 pro-PAN analytical spectra with Cu Kα radiation (K = 1.54 °A). Functional groups present in the as-prepared nanocomposites were characterized through Fourier transform infrared spectroscopy (JASCO FT-IR/6600). The structural fingerprint regions were studied with the help of WITech CRM200 confocal microscopy of the Raman system with a 488 NM laser. The structural morphology and elemental analysis were done by high-resolution transmission electron microscope FEI TECNAI T20 G2 attached with energy dispersive X-ray (EDX). Electrochemical methods such as electrochemical impedance spectroscopy (EIS), CV, and DPV were performed using the CHI 660E model from the USA. Electrocatalytic and analytical measurements were performed with a three-electrode system consisting of Ag/AgCl as a reference electrode, platinum wire as a counter electrode, and electrocatalyst-modified glassy carbon electrode (GCE) as a working electrode.

2.2. Synthesis of MoO₃/*f*-MWCNTs Nanocomposite and electrode modifications

For a typical procedure, 30 mL of 1 M sodium molybdate was mixed continuously with 5 mL H_2O_2 solution for 30 minutes to form a homogeneous suspension. Afterward, 100 mL of HNO_3 was slowly added to the reaction mixture before being transferred to a Teflon beaker and autoclaved with a double-lined stainless steel tube. The setup was kept in a hot air oven at 180°C for 12 hours during the experiment. After the reaction completion, the hydration process minimized by means of an autoclave setup was cooled down to room temperature, and the solution was washed repeatedly with DD water and then rinsed with absolute ethanol 3 times. The obtained product, MoO_3, was dried in a hot air oven at 60°C for 12 hours [31]. The acid functionalization method was used for the preparation of *f*-MWCNTs, as reported early [**41**]. In brief, about 0.5 g of MWCNTs were stirred with a 1:3 ratio of 40 mL of HNO_3/H_2SO_4 acid mixture at 50°C under continuous magnetic stirring for 8 h. Finally, the resultants were washed and centrifuged with plenty of water until the

neutral pH (7.0) was reached. The obtained black precipitate was dried in a hot air oven at 80°C for 12 h. The MoO$_3$/f-MWCNTs nanocomposite was prepared using the sonochemical methodology, in which MoO$_3$ and f-MWCNTs (1:1 ratio) were dispersed in 1 mL of DD water using a 30 min ultrasonic treatment. **Scheme 1** shows the schematic representation for the detailed synthesis procedure of MoO$_3$ nanorods (A), f-MWCNTs (B), and MoO$_3$/f-MWCNTs nanocomposite (C).
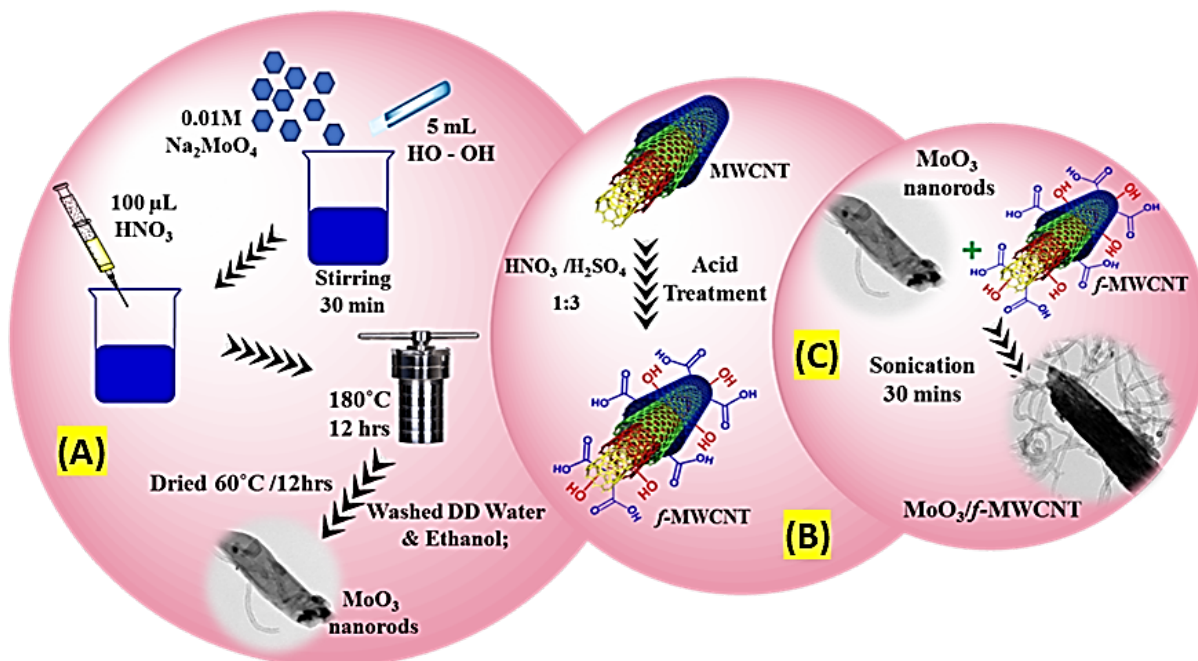
Scheme 1. The detailed synthesis procedure for MoO$_3$ nanorods (A), f-MWCNTs (B), and MoO$_3$/f-MWCNTs nanocomposite (C).

The unmodified GCE surface was cleaned using an alumina powder with the help of a polishing kid. Then, the pre-cleaned GCE was rinsed with DD water and sonicated for 3 minutes in a water/ethanol mixture. About 8 µL of the as-prepared MoO$_3$/f-MWCNTs nanocomposite was dropped on the pre-cleaned GCE surface and dried at an ambient temperature. Then, the MoO$_3$/f-MWCNTs nanocomposite GCE was gently dipped for few times and rinsed with DI water to remove loosely attached composites on the electrode surface. The as-prepared electrode was used for further electrochemical studies and stored at room

temperature. A similar procedure was adopted to fabricate MoO_3 and f-MWCNTs modified GCEs, in which 4 µL of MoO_3 and f-MWCNTs coatings were used on the GCE.

3. Results and Discussion

3.1. Physical, structural, and morphological analysis

The crystal structure, phase compositions, and purity of f-MWCNTs (a), MoO_3 (b), and MoO_3/f-MWCNTs nanocomposite (c) were studied using XRD. As shown in **Fig. 1A**, the well-defined diffraction peaks at 26.55º and 43.20º correspond to the (002) and (110) planes of f-MWCNTs, as reported elsewhere [45]. The obtained results are correlated with JCPDS data (00-026-1076) of a hexagonal phase arrangement of nanotubes. Meanwhile, pristine MWCNT shows peaks of 42.5°, 43.7°, 53.6°, and 77.6° that correspond to the (0 0 2), (1 0 0), (1 0 1), (0 0 4), (1 110) planes of the catalytic impurities present on the surface of pristine MWCNT, as we reported previously [46]. Additionally, those above diffraction peaks related to impurities were not observed on the XRD pattern of f-MWCNTs, indicating MWCNT's acid functionalization has been successful. On the other hand, the XRD analysis of MoO_3 shows prominent diffraction peaks at 12.79º, 23.37º, 25.64º, 27.40º, 33.75º, 35.49º, 38.94º, 46.06º, 49.36º, 52.71º, 55.24º, 56.30º, 58.88º, 64.75º and 69.67º and the corresponding lattice planes (020), (110), (040), (021), (111), (041), (060), (210), (002), (211), (112), (042), (081), (190) and (202) ascribed to confirm the formation MoO_3. According to these results, orthorhombic crystals are strongly associated with JCPDS data (00-005-0508) without any impurities [47]. Based on the above-obtained values, the MoO_3/f-MWCNTs nanocomposite contains both f-MWCNTs and MoO_3 diffraction patterns, confirming the formation of the MoO_3/f-MWCNTs nanocomposite. Furthermore, no peaks related to impurities in the MoO_3/f-MWCNTs nanocomposite confirmed its pure form.
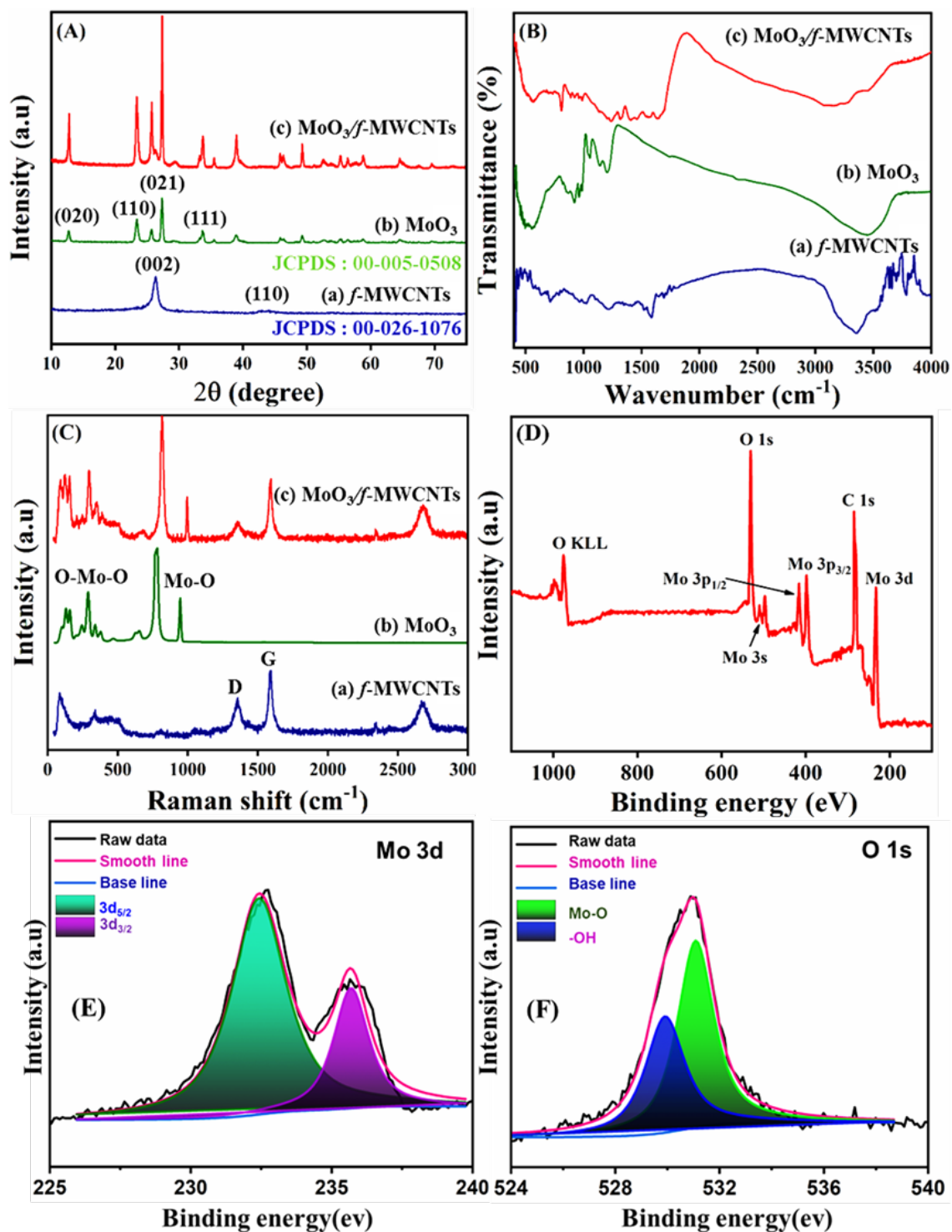
Figure 1. (A) XRD patterns (B) FT-IR spectrum and (C) Raman spectrum of (a) *f*-MWCNTs, (b) MoO_3, and (c) MoO_3/*f*-MWCNTs nanocomposite (D) XPS survey spectrum of MoO_3/*f*-MWCNTs nanocomposite. D) High-resolution XPS spectra Mo (E) and O (F).

Functional groups present in as-synthesized nanocomposite were studied using FTIR spectroscopy. The observed results for f-MWCNTs (a), MoO_3 (b), and MoO_3/f-MWCNTs nanocomposite (c) are displayed in **Fig. 1B**. For f-MWCNTs, the strong peak for C=C obtained in 1537, 1600 cm^{-1}, and the peaks at 1775 and 1307 cm^{-1} resemble C–O–C and C–O, which confirms the successful functionalization of MWCNTs. The peak obtained at 2921 cm^{-1} is attributed to the (C-H) vibration of f-MWCNTs. The presence of stretching vibrations of OH in carboxyl groups was observed at 3401-3414 cm^{-1}. For the FTIR spectrum of MoO_3, additional peaks were obtained at 971 and 908 cm^{-1} attributed to the stretching vibration of Mo = O. Also, the symmetric and asymmetric vibration of the Mo-O-Mo bond was obtained at 525 cm^{-1}. These characteristic features confirm the formation of as-synthesized MoO_3 in a hexagonal structure [48]. An FTIR spectrum of the nanocomposite showed a new bond at 809 cm^{-1}, confirming that f-MWCNTs were interlocked with MoO_3 in a stacking arrangement. The as-synthesized composite material was analyzed by Raman spectroscopy to confirm fingerprint regions and band formation. The Raman spectrum of the as-prepared f-MWCNTs, (a), MoO_3 (b), and MoO_3/f-MWCNTs nanocomposite (c) are shown in **Fig. 1C**. In graphitic materials, the G band is associated with the stretching mode of sp^2 carbon atoms. On the other hand, the D band is characterized by sp^3 hybridized carbon, which lacks in-plane symmetry with graphene. The ratio between the I_D and I_G bands is commonly used to determine the degree of disorder of graphitic materials [49]. The f-MWCNTs have two prominent peaks at 1352 and 1590 cm^{-1}, corresponding to defect-rich graphitic carbon (D band) and bonded carbon's sp2 vibration mode (G band). According to our earlier report, the I_D/I_G intensity ratio of pristine MWCNT has a higher degree of structural disorder (amorphous carbon) than f-MWCNT [46]. Additionally, decreased D and increased G bands are observed on f-MWCNT, indicating increased graphitic ordering [46]. The Raman spectrum of MoO_3 has an intensity peak at 997 cm^{-1} ascribed to the stretching vibration of the Mo-O bond. Also, the peak at 821 cm^{-1} is attributed to the formation of intermediate bridging of the O-Mo-O bond. The broad peak observed at 681 cm^{-1} corresponds to the asymmetric stretching vibration bond of Mo-

O-Mo and the bonds at 40-319 cm^{-1} due to several bending vibrations [29]. Further, the MoO_3/f-MWCNTs nanocomposite contains both the fingerprints of f-MWCNTs and MoO_3.

The elemental confirmation and oxidation state of the elements present in the prepared MoO_3/f-MWCNTs nanocomposite were documented with the help of XPS, and the obtained XPS survey spectrum is displayed in **Fig. 1D**. The survey spectrum proved that Mo, O, and C elements are present in the MoO_3/f-MWCNTs nanocomposite. The emission peaks of C 1s at a binding energy of 284.2 eV are intensive and confirm the formation of f-MWCNT. The Mo 3d oxidation states are finely divided into the Mo $3d_{3/2}$, and $3d_{5/2}$ orbitals of molybdenum (VI) positioned at 235.7 and 232.6 eV binding energies, correspondingly ascribed to the existence of hexavalent molybdenum categories (MoO_3) in the prepared nanocomposite. Additionally, the C 1s and O 1s peaks display asymmetrical shapes owing to the oxygen functionalities that covalently accompany the surface of carbon atoms of the f-MWCNT. The O 1s core-level spectrum can be split into deconvoluted constituents such as Mo-O bonds in the binding energy of 530.4 eV and C-O bonds at 532.3 eV. **Fig. 1E and F** illustrate the high-resolution XPS spectra of Mo 3d and O 1s. The Mo3d spectra show two peaks at 233.9 and 237.3 eV related to Mo $3d_{5/2}$ and Mo $3d_{3/2}$ binding energy, respectively. In addition, O 1s spectra showed peaks at 530.3 and 532.2 eV, attributed to oxygen atoms in the lattice of MoO_3. It was found that binding energy values observed with spin–orbit splitting of 3.4 eV indicated the presence of oxidized Mo (VI). These characteristics proposed that the carbon atom of f-MWCNT is probably attached to the oxygen atom in the MoO_3 [50].

The structural morphology of the as-synthesized MoO_3, f-MWCNTs, and MoO_3/f-MWCNTs nanocomposite was examined using TEM and displayed in **Fig. 2**. Typical tubular morphology was observed in the TEM image of pristine MWCNTs (A) and f-MWCNTs (B). The TEM image of MoO_3 (C) appeared as a multilayer stack rod-like structure built from planar nanoplates. A stack of MoO_3 rods with a length of 1–3 m and a diameter of 50 nm was visible on the surface of the f-MWCNT in the TEM image of the nanocomposite (D). The HRTEM image of a MoO_3/f-MWCNTs nanocomposite reveals compact

arrangements of MoO_3 nanorods on *f*-MWCNT surfaces and a d-spacing between the orthorhombic MoO_3 planes (200) and (002) with nanobelt growth occurring in the [001] direction.
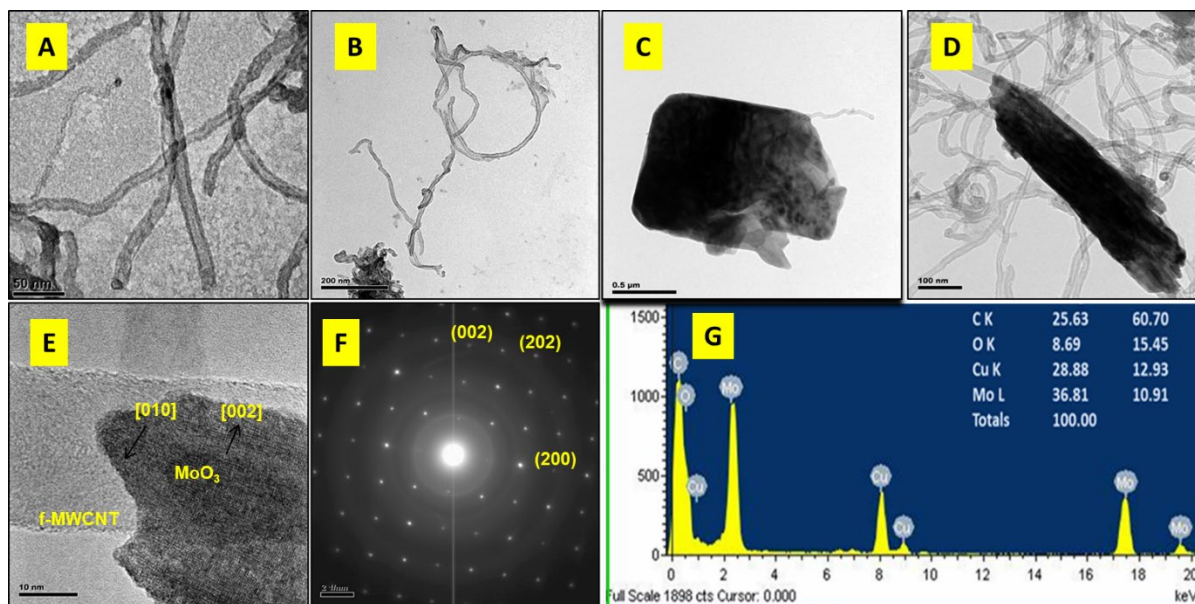

Figure 2. TEM images of MWCNTs (A), *f*-MWCNTs (B), MoO_3 (C), and MoO_3/*f*-MWCNTs (D and E). F) The SAED pattern and EDX spectra (G) of MoO_3/*f*-MWCNTs nanocomposite.

Also, the nanocomposite's HRTEM and the corresponding SAED patterns (**Fig. 2E**) confirmed the single-crystal nature of as-synthesized MoO_3. The SAED patterns confirmed the presence of (002), (202), and (200) crystallographic planes, classified as orthorhombic MoO_3. Results from the above analysis agree with those from the XRD analysis. Despite maintaining individualistic structural integrity, the constant connectivity between MoO_3 and *f*-MWCNT actively transfers electrons. Additionally, the EDX spectra of the nanocomposite were examined using EDX; as shown in **Fig. 2H**, the observed signals indicate the presence of Mo, O, and C with atomic weight percentages of 36.81%, 28.88%, 8.69%, and 25.63%, respectively. These results are consistent with the XRD and FT-IR results and show MoO_3/*f*-MWCNTs nanocomposite to be the purest form.

3.2. Electrochemical Properties of MoO_3/*f*-MWCNT nanocomposite

Electrochemical impedance spectroscopy (EIS), cyclic voltammetry (CV), and differential pulse voltammetry (DPV) were employed to evaluate the electrocatalytic properties of the as-synthesized MoO_3/f-MWCNTs nanocomposite. Various electrodes were fabricated and evaluated using EIS to determine the charge transfer resistance (R_{ct}). An electrode's total impedance equals the R_{ct} when the double-layer capacitance (C_{dl}) and Warburg impedance (Z_w) are added together. The EIS was performed using a three-electrode system containing 5 mM $[Fe(CN)_6]^{3-/4-}$ in 0.1 M KCl at a fixed potential of 10 mV. **Fig. 3A** shows the Nyquist plots of the various modified electrodes, such as bare GCE, MoO_3/GCE, f-MWCNTs/GCE, and MoO_3/f-MWCNTs/GCE. From these Nyquist plots, the R_{ct} values of bare GCE, MoO_3/GCE, f-MWCNTs/GCE, and MoO_3/f-MWCNTs/GCE were calculated as 250 Ω, 1591 Ω, 58 Ω, and 34 Ω, respectively. Notably, the bare GCE has an Rct of 250 Ω, indicating the excellent surface conductivity of the electrode. MoO_3/GCE displays a higher R_{ct} value of 1591 Ω and is higher than f-MWCNTs/GCE (58 Ω) and MoO_3/f-MWCNTs/GCE (34 Ω). This is due to the more significant availability of oxygen functions on the materials, resulting in inferior charge transport performances. However, the R_{ct} value of MoO_3/f-MWCNTs/GCE is much lower (34 Ω) than that of f-MWCNTs/GCE. By incorporating nano rod-like morphology over the f-MWCNTs, tight binding and synergistic interactions are achieved, enhancing electron transferability between electrolyte and electrode surfaces. As a result of the higher diffusion properties of MoO_3/f-MWCNTs, the modified GCE demonstrated good electrical conductivity and is more suitable for the electrochemical detection of PTZ [51].
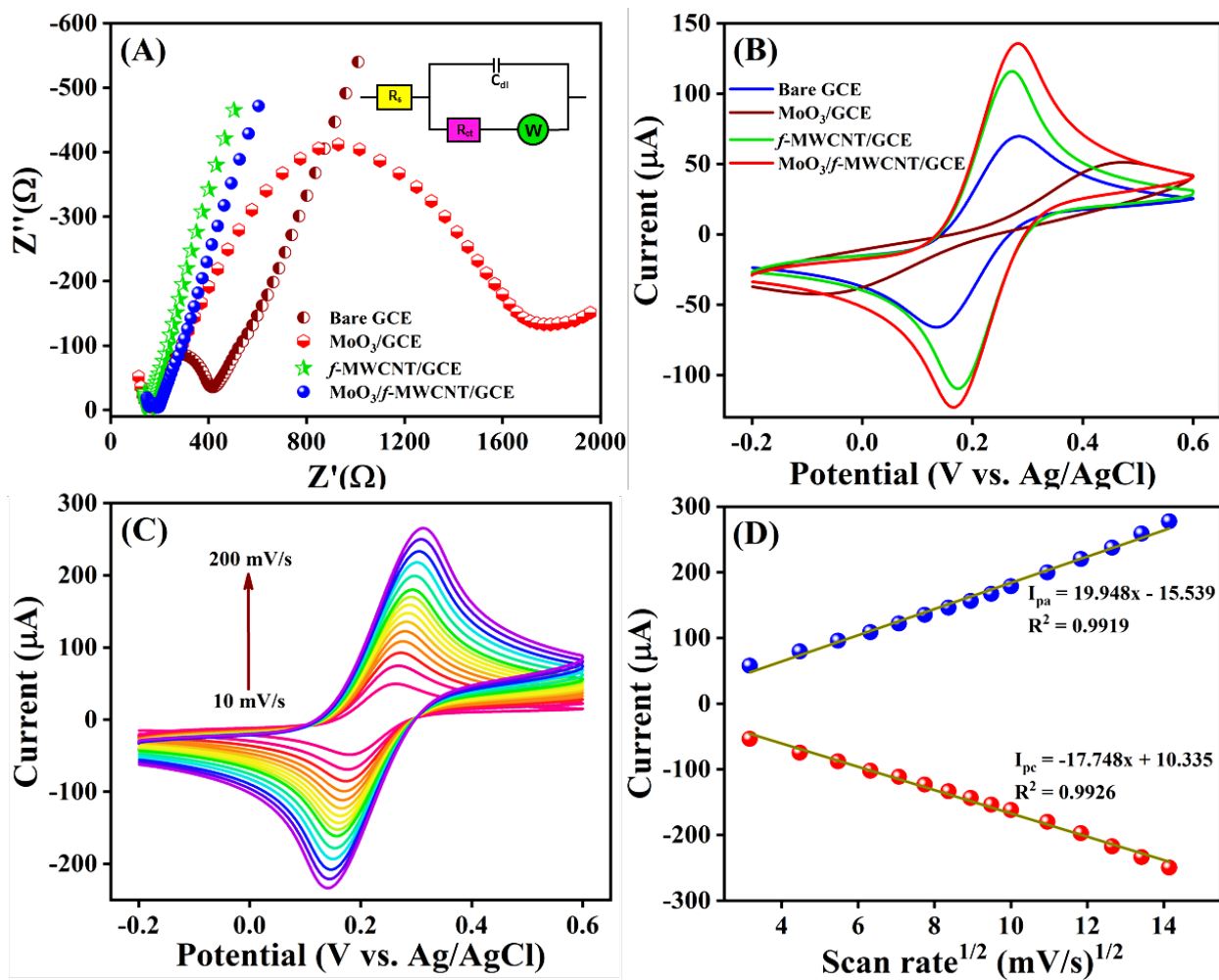
Figure 3. A) EIS and (B) CV responses of the fabricated electrodes in the presence of 5 mM $[Fe(CN)_6]^{3-/4-}$ containing 0.1 M KCl solution. Inset shows the model used to fit the EIS data. C) CV responses of MoO₃/*f*-MWCNTs nanocomposite GCE at various scan rates (10 – 200 mV/s) and (D) Linear plot for redox peak current vs. square root of scan rate.

The electrochemical activity of the as-synthesized and MoO₃/*f*-MWCNTs nanocomposite was examined further using CV in the presence of 5 mM [Fe [Fe(CN)₆]³⁻/⁴⁻ containing 0.1 M KCl solution as shown in **Fig. 3B**. When compared to MoO₃/GCE, the bare GCE exhibits better peak to peak separation, which was explained by the cleanness of the surface, which promotes electron migration to the electrode-electrolyte interface and produces pseudo-reversible nature. The MoO₃/GCE, on the other hand, has a shallow peak-to-peak separation and a weak redox couple due to the oxygen moieties and lattice vacancies present, which

14

Compared with these modified electrodes, MoO$_3$/*f*-MWCNTs/GCE has the highest redox peak response (130 µA) with a lower peak-to-peak potential (ΔEp) of 118 mV owing to higher active sites and excellent electron transfer. Electrochemical active surface area (ECAS) of the MoO$_3$/*f*-MWCNTs/GCE was calculated from CV responses of [Fe (CN)$_6$]$^{3-/4-}$ with various scan rates from 10 to 200 mV/s (**Fig. 3C**). **Fig. 3D** shows the linear relationship between peak currents and the square root of scan rates, indicating robust redox peak responses and excellent linearity for MoO$_3$/*f*-MWCNTs/GCE. The Randles-Sevcik equation (below) was used to estimate the ECAS for various modified and bare electrodes.

$$Ip = (2.69 \times 10^5)\, n^{3/2}ACD^{1/2}u^{1/2}$$

Using this equation, the ECAS for MoO$_3$/*f*-MWCNTs/GCE, MoO$_3$/GCE, and *f*-MWCNTs/GCE were calculated to be 0.401 cm^2, 0.163 cm^2, and 0.221 cm^2, respectively. ECAS values for nanocomposite-modified electrodes are higher than those for other modified electrodes because of the high electron transfer properties of the nanocomposite and enlarged active sites. Synergistic interactions between *f*-MWCNTs and MoO$_3$ produce improved electrochemical properties due to their distinct nanostructured counterparts. Thus, the MoO$_3$/*f*-MWCNTs/GCE can be used to detect PTZ more effectively.

3.3. Electrochemistry of PTZ at MoO$_3$/*f*-MWCNTs/GCE

The electrochemical oxidation of PTZ was studied at a 50 mV/s scan rate using various modified electrodes in pH 3. **Fig. 4A** illustrates the typical CV pattern for the redox behavior of PTZ using MoO$_3$/*f*-MWCNTs/GCE. Anodic peaks at 0.492 V for O$_1$, 0,92 V for O$_2$, 0.383 V for O$_3$, and 0.175 V for O$_4$ have corresponding peak current responses of 7.303, 6.04, 4.08, and 2.92 µA, respectively. The equivalent cathodic peaks were also observed at 0.471, 0.37, and 0.152 V, corresponding to cathodic peak current responses of -2.793, -3.121, and -5.831 µA, respectively. As a result of the removal of one electron from

nitrogen and the sequential ejection of a second electron from sulfur, the O_1, and O_2 peaks were formed (**Scheme 2**). The reversible nature of peak O_1 made it possible to see the cathodic peak R_1 during the reverse scan. Additionally, O_3, O_4, R_2, and R_3 were associated with readily oxidized molecules formed by the oxidation of PTZ. CV patterns for *f*-MWCNTs/GCE and MoO_3/GCE are similar, with slight variations in peak potential and current response.
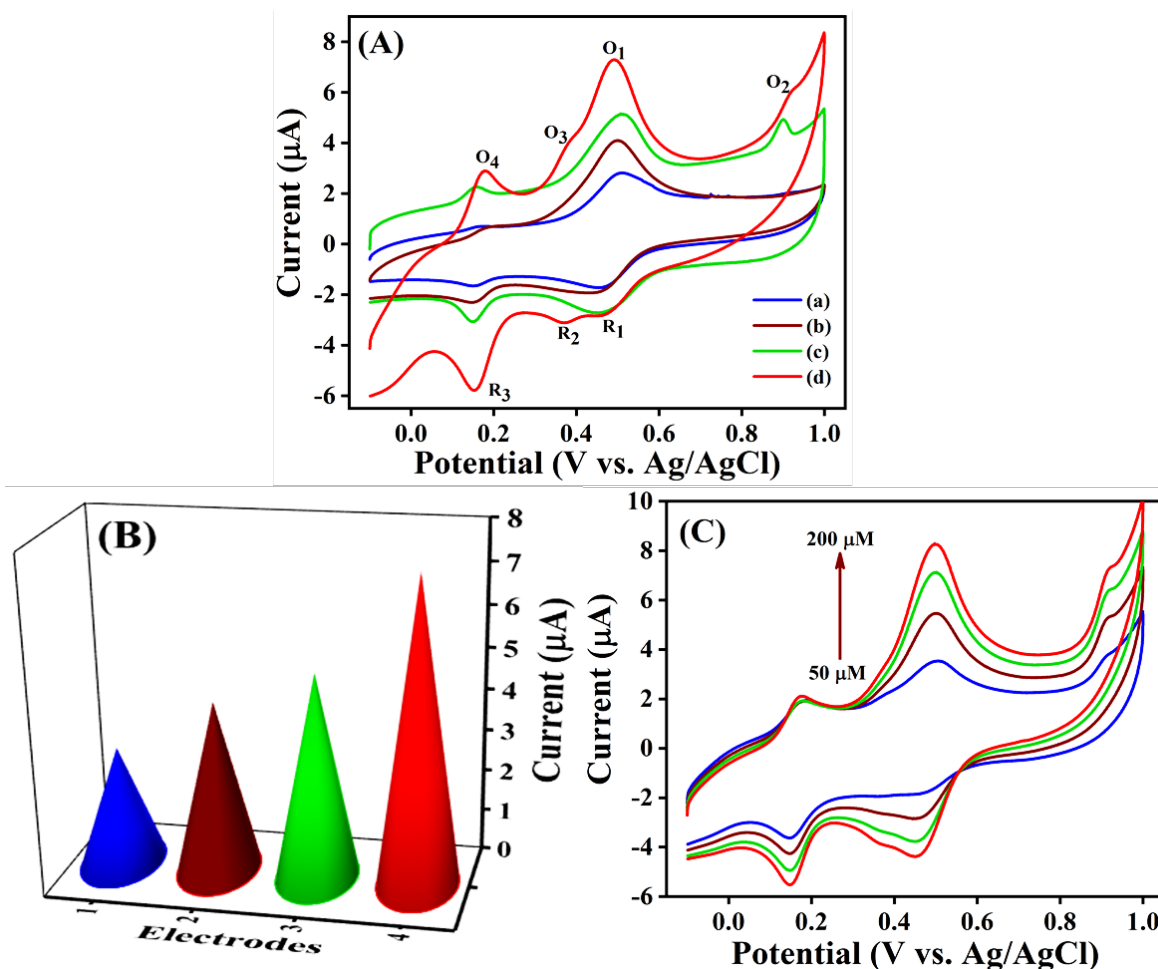

Figure 4. A) CV response of bare (a), MoO_3 (b) *f*-MWCNTs (c), and MoO_3/*f*-MWCNTs (d) modified GCEs in pH 3.0 in the presence of PTZ (200 μM), and B) the corresponding bar graph for the current responses obtained on bare (1), MoO_3 (2) *f*-MWCNTs (3) and MoO_3/*f*-MWCNTs (4) modified GCEs. C) CV responses were obtained for the MoO_3/*f*-MWCNTs/GCE in various concentrations of PTZ (50–200 μM).

While the oxidation peak current of PTZ on bare GCE was 1.6 folds lower than those observed using *f*-MWCNTs/GCE [11]. **Fig. 4B** shows the corresponding bar charts for the oxidation peak responses of PTZ on various modified electrodes. The MoO_3/*f*-MWCNTs/GCE has higher catalytic activity towards PTZ than other modified electrodes. We examined the catalytic activity of a modified electrode for detecting varying concentrations of PTZ. As shown in **Fig. 4C**, the modified GCE with MoO_3/*f*-MWCNTs exhibits well-defined redox for 50 µM PTZ addition, and anodic and cathodic current increases with increasing PTZ addition. According to CV results, the modified electrode demonstrated excellent electrocatalytic activity towards PTZ. Additionally, the redox peak current vs. PTZ concentration calibration plot can be written as I_{pa} = 0.0316x + 2.12; I_{pc} = -0.0174x - 1.065, and the correlation coefficients (R^2) are 0.9925 and 0.9916, respectively. A linear plot slope indicates that PTZ's oxidation is governed by first-order reaction kinetics.
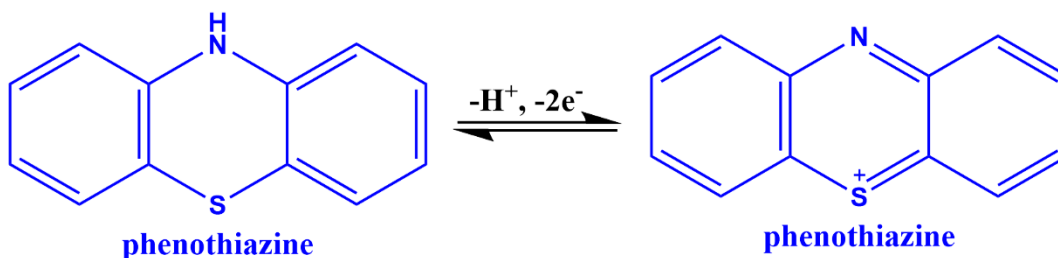
Scheme 2. Electrochemical redox pathway of PTZ on MoO_3/*f*-MWCNTs modified GCE.

3.4. Effect of scan rate and supporting pH

The electrochemical determination of PTZ is heavily influenced by scan rate. Hence, the MoO_3/*f*-MWCNTs modified GCE was analyzed using scan rates ranging from 10 to 300 mV/s in pH 3 with 200 µM PTZ. According to **Fig. 5A**, the scan rate and redox peak currents increase linearly with slight potential changes. Moreover, it has been confirmed that PTZ is detectable by electrocatalysis reversibly. Furthermore, **Fig. 5B** shows calibration plots for redox peak current responses as a function of scan rate with linear regression equations I_{pa} = 0.0819x + 2.5954; I_{pc} = -0.0434x − 0.37 and R^2 of 0.9952 and 0.9986,

respectively. From these results, we can conclude that the electrochemical analysis of MoO_3/f-MWCNTs/GCE was surface controlled electrochemical process.
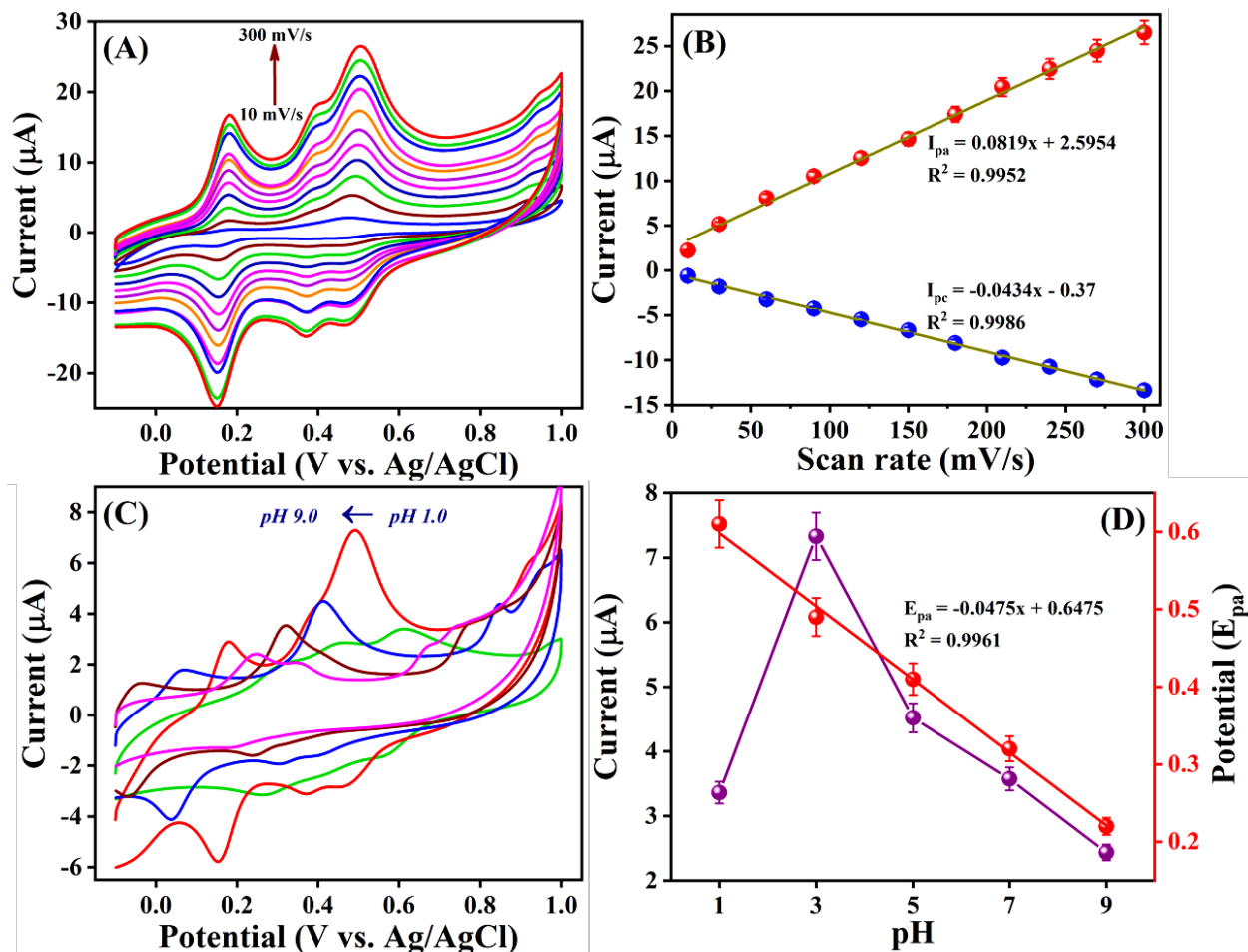

Figure 5. A) CV response of MoO_3/f-MWCNTs/GCE at different scan rates in 200 µM PTZ. B) Calibration plot of redox peak current vs. scan rate. C) CV curve of modified electrode for 200 µM PTZ at different pH at a scan rate of 50 mV/s, and D) the corresponding combined plot of pH vs. PTZ peak current and peak potential of MoO_3/f-MWCNTs/GCE.

The pH of the electrolyte solution affects the electrochemical performance of MoO_3/f-MWCNTs/GCE towards sensing of PTZ. In addition, PTZ shapes, potentials, and characteristic peak currents are all influenced by the pH of the electrolyte. Therefore, pH measurements were used to identify the electrochemical determination of PTZ at MoO_3/f-MWCNTs/GCE. As shown in **Fig. 5C**, the effects of pH were

investigated using pHs ranging from 1.0 to 9.0 at 50 mV/s sweep rates. As can be seen that the peak current gradually increases from 1.0 to 3.0 after 3.0 to 9.0 and then decreases due to the existence of heterocyclic ring compounds. Likewise, **Fig. 5D** displays the combined plot for pH vs. peak current and peak potential. As a result of these results, we selected pH 3.0 as the best pH for all electrochemical experiments since the high peak current occurred at pH 3.0 with a narrow peak potential.

3.5. Electrochemical determination of PTZ at MoO$_3$/*f*-MWCNTs/GCE

The DPV technique is an efficient tool for analyzing biological compounds at a low level. The electrocatalytic performance of MoO$_3$/*f*-MWCNTs/GCE towards the determination of PTZ was analyzed with the help of the DPV. **Fig. 6A** shows the DPV curves of MoO$_3$/*f*-MWCNTs/GCE in pH 3.0 with PTZ concentrations from 0.1 µM to 226 µM. With increasing concentrations of PTZ, the peak current response to oxidation increases. **Fig. 6B** shows the calibration plot for the concentration of PTZ against the oxidation peak current. This calibration plot illustrates the broad dynamic response range with a linear regression equation I_{pa} = 0.0378x + 0.6181 and an R^2 = 0.9949. Calculation of the detection limit (LOD) and sensitivity for electrochemical oxidation of PTZ is based on the slope value found on the calibration plot. Based on the equation below, the LOD was calculated.

$$LOD = 3\sigma/S \tag{1}$$

Based on the calibration plot, S represents the slope, and σ represents the standard deviation (S/N = 3). As a result of the above equation, the LOD and sensitivity for MoO$_3$/*f*-MWCNTs/GCE are calculated to be 7 nM and 4.712 µAµM^{-1} cm^{-2}, respectively.
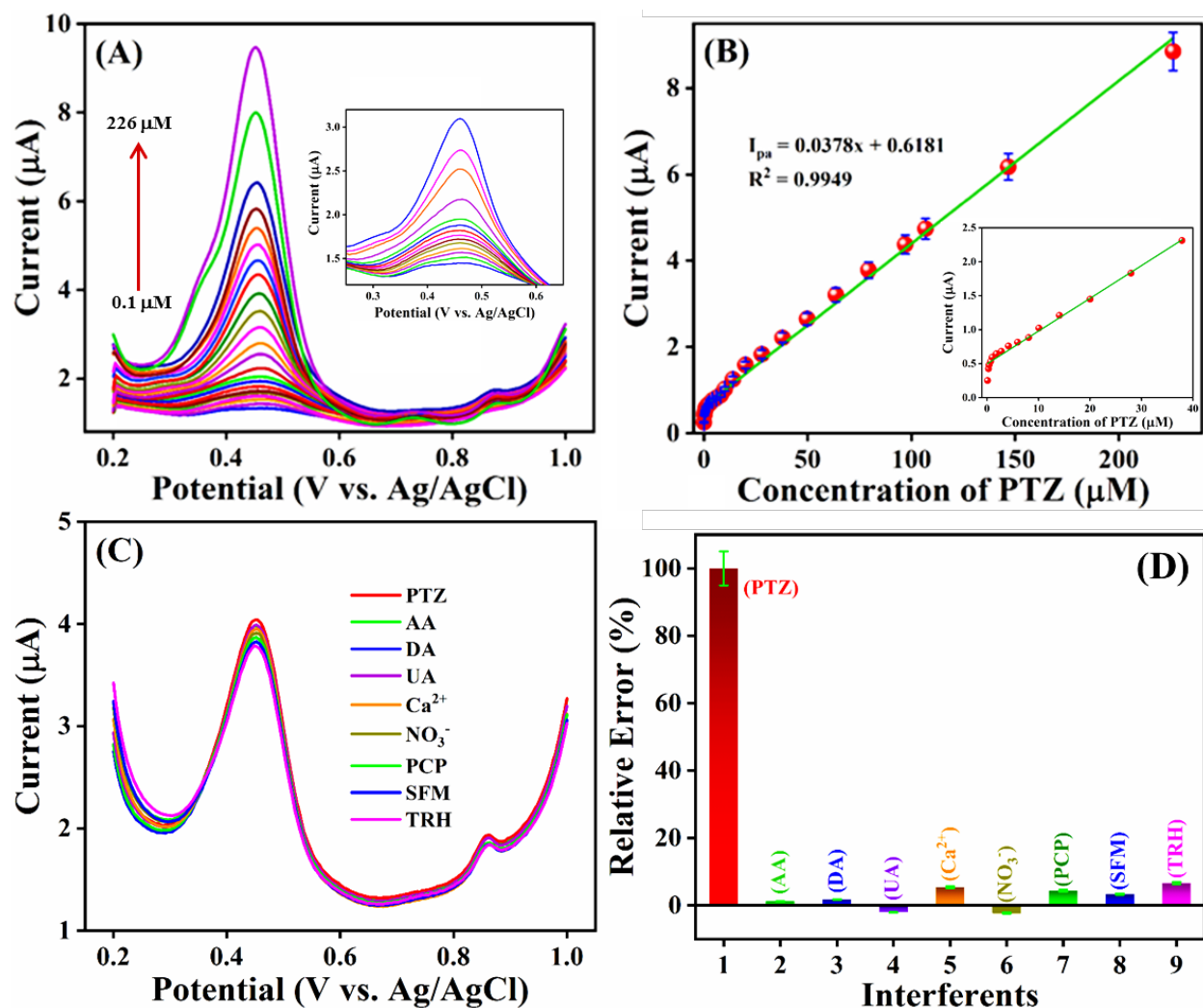
Figure 6. A) DPV responses of MoO$_3$/f-MWCNTs/GCE upon the successive addition of PTZ concentration (0.01− 226 μM) in pH 3.0. Inset is the lower concentration additions of PTZ up to 50 μM. B) The calibration plot of oxidation peak current vs. [PTZ]. Linear plot for [PTZ] up to 38 μM vs. current response (inset). C) DPV response of MoO$_3$/f-MWCNTs/GCE toward PTZ in the presence of an excess concentration of co-interfering compounds and D) corresponding relative error bar graph of interfering compounds vs. relative peak current in percentage.

Moreover, the obtained LOD, wide dynamic response range and sensitivity are correlated with formerly reported electrochemical determinations towards PTZ, as summarized in **Table 1**. According to these table results, MoO$_3$/f-MWCNTs/GCE exhibits lower LOD, a wider dynamic range, and excellent

sensitivity toward PTZ sensing than previously reported modified electrodes based on carbon nanomaterials and metal oxide composites [14, 52-55].

Table 1. Comparison of analytical merits of the fabricated PTZ sensor with previously reported PTZ sensors.

Materials	Methods	Linear Range (µM)	LOD (µM)	Ref
f-CNF/Er_2MoO_6	DPV	0.025 – 80	0.008	[14]
GZO/*f*–SWCNT	DPV	0.01 – 98.51	0.05	[52]
MWCNT−OSO_3H	Amperometry	0.62– 5000	0.15	[53]
FTO	Amperometry	2.0– 100	0.26	[54]
DyCoO_3/MoS_2	DPV	0.002– 695.6	0.05	[55]
MoO_3/*f*-MWCNT	DPV	0.01 − 226	0.007	**This Work**

3.6. Selectivity of the PTZ sensor at MoO_3/*f*-MWCNTs/GCE

Based on anti-interference property studies, the practical applicability of the proposed sensor was optimized. The DPV technique scrutinized the selectivity of the MoO3/f-MWCNTs/GCE, and the observed DPV results are displayed in **Fig. 6C**. Selectivity studies are conducted using a variety of interfering species, including similar structural materials, biological compounds, and anionic and cationic molecules. We added 10-fold excess concentrations of biological compounds such as ascorbic acid (AA), dopamine (DA), and uric acid (UA) to evaluate the selectivity studies. Likewise, a 20-fold excess of cation and anion and similar structured species such as Ca^{2+}, NO_3^-, prochlorperazine (PCP), sulfamethoxazole (SFM), and thioridazine hydrochloride (TRH) was also investigated. **Fig. 6D** illustrates the corresponding relative peak current percentage vs. potential interfering compounds. A similar structural material or biological compound and anionic or cationic molecules did not affect PTZ's DPV response. The results support the use of MoO_3/*f*-MWCNTs for selective detection of PTZ.
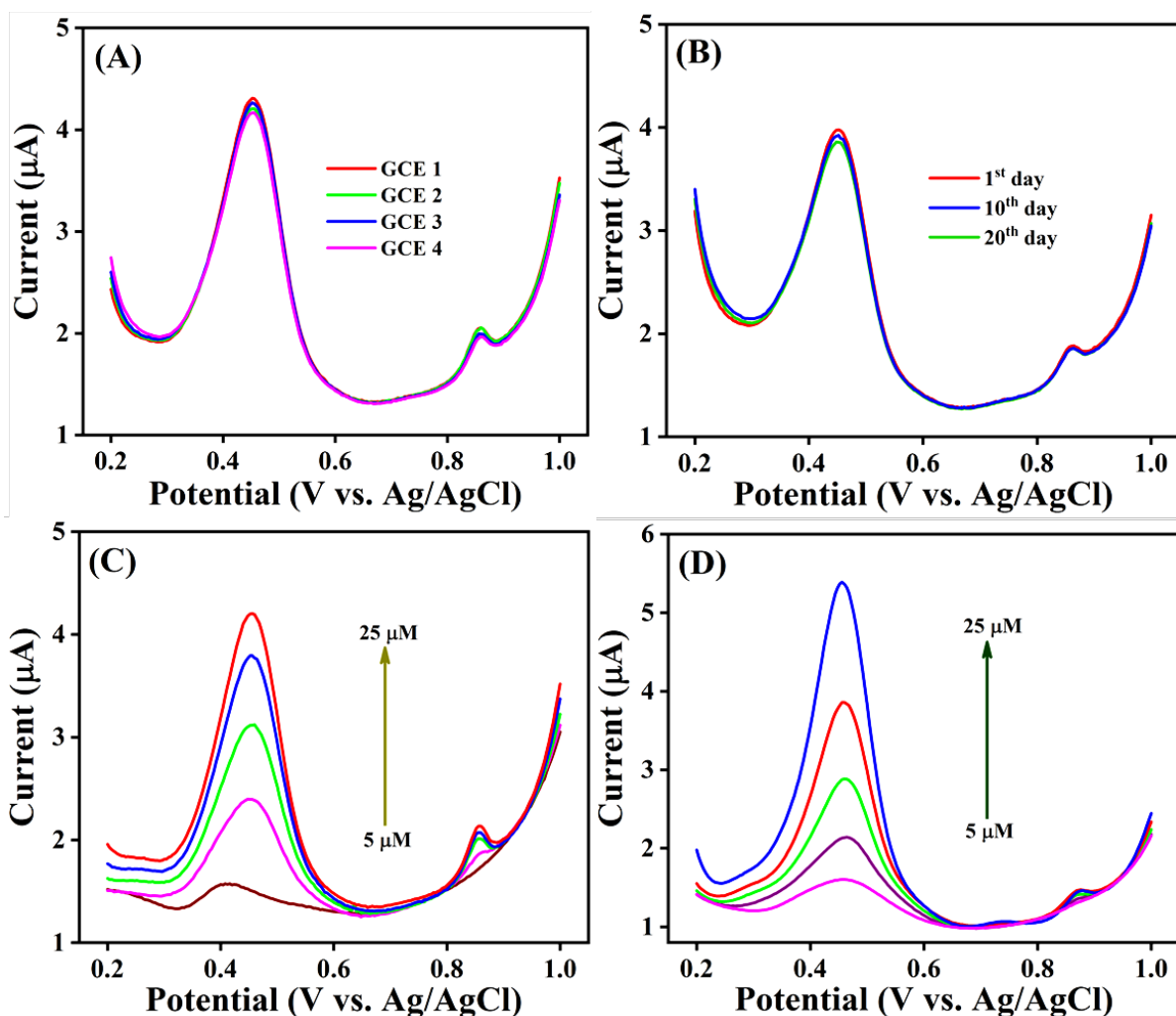
Figure 7. DPV responses of (A) reproducibility and B) storage stability of the fabricated PTZ sensor for response to 50 µM PTZ in pH 3.0. DPV signals for determining PTZ in the C) human blood serum and D) urine samples.

3.7. Reproducibility and Real sample analysis

A reproducibility study was conducted using four different versions of MoO$_3$/f-MWCNTs modified electrodes in the presence of 50 µM PTZ in pH 3, and the observed results are shown in **Fig. 7A**. The relative standard deviation (RSD) was determined to be 2.38. This indicates a reasonable reproducibility of the prepared MoO$_3$/f-MWCNTs/GCE concerning the PTZ sensor. A further evaluation of the proposed sensor's storage capability was carried out by DPV in 50 µM PTZ containing pH 3, and the results are shown in **Fig. 7B**. The

We investigated whether MoO$_3$/*f*-MWCNTs/GCE could be used to measure PTZ in real biological samples such as human blood serum and urine samples. Blood serum and urine samples were collected from a healthy individual and did not contain PTZ traces. The pH of the received human serum and urine samples was initially adjusted to 3.0 by diluting them. A known concentration of PTZ was spiked into diluted solutions during real-sample analysis. **Fig. 7C** and **D** illustrate the DPV responses for PTZ detection in human blood serum and urine samples using the standard addition method. Based on the results found in **Table 2**, we could determine the concentration and recovery of PTZ. Using the Table, we found that human blood serum could be recovered with 97.5-99.6 % accuracy, and human urine could be recovered with 94.6-99.8 % accuracy with an RSD of 2.3%. Our findings demonstrate the suitability of the proposed sensor for practical applications.

Table 2. Determination of PTZ in human blood serum and urine samples.

Sample	Added (µM)	Found (µM)	Recovery (%)
Human blood serum	5	4.97	99.4
	10	9.75	97.5
	15	14.87	99.1
	20	19.80	99.0
	25	24.90	99.6
Human urine	5	4.88	97.6
	10	9.46	94.6
	15	14.95	99.7

	20	19.90	99.5
	25	24.96	99.8

4. Conclusion

In conclusion, a very efficient hydrothermal technique, followed by ultrasonication, was used to create the MoO$_3$/f-MWCNTs nanocomposite. The structural purity and morphological analysis were assessed using XRD, FTIR, Raman, HR-TEM, and EDX techniques. The results show that MoO$_3$/f-MWCNTs nanocomposites can be produced effectively without any impurities. The MoO$_3$/f-MWCNTs modified GCE showed better electrocatalytic response towards PTZ detection, which has a low detection limit and a broad linear response range than previously reported carbon nanomaterials composite-based modified electrodes. In addition, the suggested sensor displays acceptable repeatability, stability, and exceptional selectivity in the presence of biological substances. Furthermore, real samples such as human blood and urine samples were used to assess the practical feasibility of MoO$_3$/f-MWCNTs/GCE, and the observed average recovery results (99.6% & 99.8%) are satisfactory. The new nanocomposite material possesses excellent electrocatalytic determination of PTZ due to the solid hydrothermally synthesized single-crystalline MoO$_3$ nanorods embedded over f-MWCNTs. Future usage of the created MoO$_3$/f-MWCNTs nanocomposite as a sensitive electrode material for detecting PTZ in biological fluids is possible. However, the sensor has some limitations, including issues with the selective detection of PTZ when large amounts of similarly structured compounds with similar electroactivity are present.

Declaration of Competing Interest

The authors declare that they have no known competing financial interests or personal relationships that could have appeared to influence the work reported in this paper.

References

[1]   X. Jiang, S. Chen, X. Zhang, L. Qu, H. Qi, B. Wang, B. Xu, Z. Huang, Carbon-doped flower-like Bi_2WO_6 decorated carbon nanosphere nanocomposites with enhanced visible light photocatalytic degradation of tetracycline, Adv. Compos. Mater. 6 (2023) 9.

[2]   Z. Sun, Y. Zhang, S. Guo, J. Shi, C. Shi, K. Qu, H. Qi, Z. Huang, Vi. Murugadoss, M. Huang, Z. Guo, Confining FeNi nanoparticles in biomass-derived carbon for effectively photo-Fenton catalytic reaction for polluted water treatment, Adv. Compos. Mater. 5 (2022) 1566–1581.

[3]   X. Xie, H. Gao, X. Luo, Y. Zhang, Z. Qin, H. Ji, Polyethyleneimine-modified magnetic starch microspheres for Cd(II) adsorption in aqueous solutions, Adv. Compos. Mater. 5 (2022) 2772–2786.

[4]   R. Shanmugam, P. Barathi, J-M. Zen, A. Senthil Kumar, An unusual electrochemical oxidation of phenothiazine dye to phenothiazine-bi-1,4-quinone derivative (a donor-acceptor type molecular hybrid) on MWCNT surface and its cysteine electrocatalytic oxidation function, Electrochim. Acta. 187 (2016) 34–45.

[5]   M. J. Ohlow, B. Moosmann, Phenothiazine: the seven lives of pharmacologys first lead structure, Drug Discov. Today 16 (3–4) 119 – 131.

[6]   A. Aszalos, Phenothiazines in treatment of HIV Infection (a review), Acta Microbiol Immunol Hung. 50 (2003) 43.

[7]   Y. I. Kuzin, A. I. Khadieva, P. L. Padnya, A. A. Khannanov, M. P. Kutyreva, I. I. Stoikov, G. A. Evtugyn, Electrochim. Acta. 375 (2021) 137985.

[8]   K. Periyasamy, P. Sakthivel, G. Venkatesh, P. M. Anbarasan, P. Vennila, Y. Sheena Mary, S. Kaya, S. Erkan, Synthesis, photophysical, electrochemical, and DFT examinations of two new organic dye molecules based on phenothiazine and dibenzofuran, Journal of Molecular Modeling 28 (2022) 34.

[9]   P. Manusha, S. Yadav, J. Satija, S. Senthilkumar, Designing electrochemical NADH sensor using silver nanoparticles/ phenothiazine nanohybrid and investigation on the shape dependent sensing behavior, Sens. Actuators B Chem. 347 (2021) 130649.

[10]   E. Martínez-Peri~n'an, I. Bravo, M. Mediavilla, M. Revenga-Parra, E. Mateo-Martí, F. Pariente, E. Lorenzo, Spectroelectrochemical operando method for monitoring a phenothiazine electrografting process on amide functionalized C-nanodots/Au hybrid electrodes, Electrochim. Acta. 298 (2019) 950–959.

[11]   M. Kalkanidis, N. Klonis, L. Tilley, L.W. Deady, Novel phenothiazine an- timalarials: synthesis, antimalarial activity, and inhibition of the forma- tion of β-haematin, Biochem. Pharmacol. 63 (2002) 833–842.

[12]   J. Nordenberg , E. Fenig , M. Landau , R. Weizman , A. Weizman. Effects of psychotropic drugs on cell proliferation and differentiation, Biochem. Pharmacol. 58 (1999) 1229–1236.

[13]   M. Viveiros, L. Amaral, Enhancement of antibiotic activity against poly-drug resistant Mycobacterium tuberculosis by phenothiazines, Int. J. Antimicrob. Ag. 17 (2001) 225–228.

[14]   X. Liu, J-H. He, R. Sakthivel, R-J. Chung, Rare earth erbium molybdate nanoflakes decorated functionalized carbon nanofibers: An affordable and potential catalytic platform for the electrooxidation of phenothiazine, Electrochim. Acta. 358 (2020) 136885.

[15]   J. Zhou, L. Mao, M-X. Wu, Z. Peng, Y. Yang, M. Zhou, X-L. Zhao, X. Shi, H-B. Yang, Extended phenothiazines: synthesis, photophysical and redox properties, and efficient photocatalytic oxidative coupling of amines, Chem. Sci. 13 (2022) 5252-5260.

[16]   C.E. Aronson, E.R. Hanno, Effects of promethazine on the isolated perfused rat heart, Gen. Pharmacol. 10 (1979) 389–395.

[17]   C.G. Hover, A.P. Kulkarni, Human term placental lipoxygenase-mediated N-demethylation of phenothiazines and insecticides in the presence of linoleic acid, Placenta. 21 (2000) 646–653.

[18] M.C. Posso, F.C. Domingues, S. Ferreira, S. Silvestre, Development of Phenothiazine Hybrids with Potential Medicinal Interest: A Review, Molecules. 27 (1) (2022) 276.

[19] G. Facciola, M. Hidestrand, C. Von Bahr, G. Tybring, Cytochrome P450 isoforms involved in melatonin metabolism in human liver microsomes, Eur. J. Clin. Pharmacol. 56 (2001) 881.

[20] B. Blankert, H. Hayen, S.M. Van Leeuwen, U. Karst, E. Bodoki, S. Lotrean, R. San- dulescu, N.M. Diez, O. Dominguez, J. Arcos, J. M. Kauffmann, Electrochemical, chemical and enzymatic oxidations of phenothiazines, Electroanal. 17 (2005) 1501–1510.

[21] K. Farhadi, M. Shamsipur, Potentiometric and spectrophotometric determination of phenothiazine derivatives based on their titration with 2, 3- dichloro-5, 6-dicyano-1, 4-benzoquinone, Acta Chim. Slov. 50 (2003) 395-408.

[22] E. Tanaka, T. Nakamura, M. Terada, T. Shinozuka, C. Hashimoto, K. Kurihara, K. Honda, Simple and Simultaneous Determination for 12 Phenothiazines in Human Serum by Reversed-Phase High-Performance Liquid Chromatography, J. Chromatogr. B Anal. Technol. Biomed. Life Sci. 854 (2007) 116–120.

[23] P-Y. Chen, Y-M. Chi, H-H. Yang, Y. Shih, A sulfite sensor based on electrocatalytic oxidation at a phenothiazine drop-coated screen-printed carbon electrode, J. Electroanal. Chem. 675 (2012) 1–4.

[24] B. Arumugam, S.K. Ramaraj, Insights into the Design and Electrocatalytic Activity of Magnesium Aluminum Layered Double Hydroxides: Application to Nonenzymatic Catechol Sensor, Langmuir 38 (16) (2022) 4848-4858.

[25] B. Arumugam, V. Nagarajan, J. Annaraj, S.K. Ramaraj, Barium titanate nanoparticle-based disposable sensor for nanomolar level detection of the haematotoxic pollutant quinol in aquatic systems, New J. Chem., 46 (2022) 3006–3016.

[26] V. Kumar, X. Wang, P. S. Lee, Synthesis of pyramidal and prismatic hexagonal MoO_3 nanorods using thiourea, CrystEngComm, 15 (2013) 7663–7669.

[27] H. Karimi-Maleh, I. Sheikhshoaie, A. Samadzadeh, Simultaneous electrochemical determination of levodopa and piroxicam using a glassy carbon electrode modified with a ZnO–Pd/CNT nanocomposite, RSC Adv. 8 (2018) 26707–26712.

[28] L. Cai, P. M. Rao, X. Zheng, Morphology-controlled flame synthesis of single, branched, and flower-like r-MoO_3 nanobelt arrays. Nano Lett. 11 (2011) 872–877.

[29] R. Nadimicherla, W. Chen, X. Guo, Synthesis and characterization of α-MoO_3 nanobelt composite positive electrode materials for lithium battery application, Mater. Res. Bull. 66 (2015) 140–146.

[30] P. Balasubramanian, M. Annalakshmi, S-M. Chen, T-W. Chen, Sonochemical synthesis of molybdenum oxide (MoO_3) microspheres anchored graphitic carbon nitride (g-C_3N_4) ultrathin sheets for enhanced electrochemical sensing of Furazolidone. Ultrason Sonochem. 50 (2019) 96–104.

[31] B. Feng, Z. Wu, J. Liu, K. Zhu, Z. Li, X. Jin, Y. Hou, Q. Xi, M. Cong, P. Liu, Q. Gu, Combination of ultrafast dye-sensitized-assisted electron transfer process and novel Z-scheme system: AgBr nanoparticles interspersed MoO_3 nanobelts for enhancing photocatalytic performance of RhB, Appl. Catal. B. 206 (2017) 242–251.

[32] H. Deng, J. Huang, Z. Hu, X. Chen, D. Huang, T. Jin, Fabrication of a Three-Dimensionally Networked MoO_3/PPy/rGO Composite for a High-Performance Symmetric Supercapacitor, ACS Omega. 6 (2021) 9426−9432.

[33] X. Cao, B. Zheng, W. Shi, J. Yang, Z. Fan, Z. Luo, X. Rui, B. Chen, Q. Yan, H. Zhang, Reduced graphene oxide-wrapped MoO_3 composites prepared by using metal–organic frameworks as precursor for all-solid-state flexible supercapacitors, Adv. Mater. 27 (2015) 4695–4701.

[34] K. M. Mamatha, V. Srinivasa murthy, C. R. Ravikumar, H. C. Ananda Murthy, V. G. Dileep Kumar, A. Naveen Kumar, A. A. Jahagirdar, Facile green synthesis of Molybdenum oxide nanoparticles using Centella Asiatica plant: Its photocatalytic and electrochemical lead sensor applications, Sensors International 3 (2022) 100153.

[35] Kaya, S. I., B. Demirkan, N. K. Bakirhan, E. Kuyuldar, S. Kurbanoglu, S. A. Ozkan, F. Sen, Highly sensitive carbon-based nanohybrid sensor platform for determination of 5-hydroxytryptamine receptor agonist (Eletriptan), Journal of pharmaceutical and biomedical analysis 174 (2019) 206-213.

[36] N., Rupak, A. Sharma, D. Kumar, S. Mukherjee, F. Sen, A.P. Kumar, Amalgamation of biosensors and nanotechnology in disease diagnosis: mini-review, Sensors International 2 (2021) 100089.

[37] Ş. Aysun, H. Aydın, K. Cellat, F. Şen. A novel high performance non-enzymatic electrochemical glucose biosensor based on activated carbon-supported Pt-Ni nanocomposite, Journal of Molecular Liquids 300 (2020) 112355.

[38] A. Kubilay, H. Burhan, R. Bayat, F. Sen, Glucose nano biosensor with non-enzymatic excellent sensitivity prepared with nickel–cobalt nanocomposites on f-MWCNT, Chemosphere 291 (2022) 132720.

[39] X. Miao, Z. Li, S. Liu, J. Wang, S. Yang, MXenes in tribology: Current status and perspectives, Advanced Powder Materials 2 (2023) 100092.

[40] H. Yin, W. Zhong, M. Yin, C. Kang, L. Shi, H. Tang, C. Yang, J.T. Althakafy, M. Huang, A.K. Alanazi, L. Qu, Y. Li, Carboxyl-functionalized poly(arylene ether nitrile)-based rare earth coordination polymer nanofibrous membrane for highly sensitive and selective sensing of Fe^{3+} ions, Adv. Compos. Mater. 5 (2022) 2031–2041.

[41] W. Shao, J. Mai, Z. Wei, Nonenzymatic Lactic Acid Detection Using Cobalt Polyphthalocyanine/Carboxylated Multiwalled Carbon Nanotube Nanocomposites Modified Sensor, Chemosensors 10 (2022) 83.

[42] H. Bora, D. Mandal, A. Chandra, High-performance, Nitrogen-doped, carbon-nanotube-based electrochemical sensor for vitamin D3 detection, ACS Appl. Bio Mater. 5 (4) (2022) 1721-1730.

[43] N. A. Bohari, S. Siddiquee, S. Saallah, M. Misson, S. E. Arsha, Electrochemical behaviour of real-time sensor for determination mercury in cosmetic products based on PANI/MWCNTs/AuNPs/ITO. Cosmetics, 8 17 (2021) 1-15.

[44] D. Vasu, A. Karthi Keyan, S. Sakthinathan, T-W. Chiu, Investigation of electrocatalytic and photocatalytic ability of Cu/Ni/TiO_2/MWCNTs Nanocomposites for detection and degradation of antibiotic drug Furaltadone. Sci. Rep. 12 (1) (2022) 1-16.

[45] Y. F. Wang, S. X. Zhao, L. Yu, X. X. Zheng, Q. L. Wu, G. Z. Cao, Design of multiple electrode structures based on nano Ni_3S_2 and carbon nanotubes for high performance supercapacitors. J. Mater. Chem. A. 7 (2019) 7406–7414.

[46] S. Palanisamy, V. Velusamy, S. Balu, S. Velmurugan, T.C.K. Yang, S-W. Chen, Sonochemical synthesis and anchoring of zinc oxide on hemin-mediated multiwalled carbon nanotubes-cellulose nanocomposite for ultra-sensitive detection of H_2O_2, Ultrason Sonochem. 63 (2020) 104917.

[47] P. Thangasamy, N. Ilayaraja, D. Jeyakumar, M. Sathish, Electrochemical cycling and beyond: unrevealed activation of MoO_3 for electrochemical hydrogen evolution reactions, Chem. Commun., 53 (2017) 2245-2248.

[48] Y. Liu, S. Yang, Y. Lu, N.V. Podval'naya, W. Chen, G.S. Zakharova, Hydrothermal synthesis of h-MoO_3 microrods and their gas sensing properties to ethanol, Appl. Surf. Sci. 359 (2015) 114–119.

[49] P. Barathi, A.S. Kumar, Electrochemical conversion of unreactive pyrene to highly redox-active 1,2-quinone derivatives on a carbon nanotube-modified gold electrode surface and its selective hydrogen peroxide sensing, Langmuir, 29 (2013) 10617.

[50] F. Ma, A. Yuan, J. Xu, P. Hu, Porous α-MoO_3/MWCNT Nanocomposite Synthesized via a Surfactant-Assisted Solvothermal Route as a Lithium-Ion-Battery High-Capacity Anode Material with Excellent Rate Capability and Cyclability, ACS Appl. Mater. Interfaces (2015)

[51] S. M. Babulal, S-M. Chen, R. Palani, K. Venkatesh, A. S. Haidyrah, S. K. Ramaraj, C-C. Yang, C. Karuppiah, Graphene oxide template based synthesis of $NiCo_2O_4$ nanosheets for high performance non-enzymatic glucose sensor, Colloids Surf. A Physicochem. Eng. Asp. 621 (2021) 126600.

[52] S. Pulikkutty, N. Manjula, T-W. Chen, S-M. Chen, B-S. Lou, M. R. Siddiqui, S. M. Wabaidur, M. Ajmal Ali, Fabrication of gadolinium zinc oxide anchored with functionalized-SWCNT planted on glassy carbon electrode: Potential detection of psychotropic drug (phenothiazine) in biotic sample, J. Electroanal. Chem. 918 (2022) 116521.

[53] S. Mirela, M. Peršić, A. Széchenyi, M. Jozanović, I. Pukleš, M. Budetić, Development of the New Sensor Based on Functionalized Carbon Nanomaterials for Promethazine Hydrochloride Determination, Sensors 23 (2023) 2641.

[54] M-R. Francisco, C. Espinosa-Bustos, G. Ramirez, F. Armijo, Electrochemical oxidation of chlorpromazine, characterisation of products by mass spectroscopy and determination in pharmaceutical samples, Electrochimica Acta 443 (2023) 141873.

[55] K. Chelliah, R. Pandiyan, S-M. Chen, Rational design of dysprosium cobalt oxide decorated on flower-like molybdenum disulfide: Development of an electrochemical sensor for antipsychotic drug promazine, Process Safety and Environmental Protection 170 (2023) 1188-1199.